Bioactive Materials 6 (2021) 712–720

Contents lists available at ScienceDirect

Bioactive Materials

journal homepage: http://www.keaipublishing.com/biomat

Inhibition of furin by bone targeting superparamagnetic iron oxide nanoparticles alleviated breast cancer bone metastasis

Yichuan Pang[a,b,1], Li Su[c,1], Yao Fu[d], Fan Jia[e], Chenxi Zhang[c], Xiankun Cao[a], Wenxin He[a], Xueqian Kong[d], Jiake Xu[f], Jie Zhao[a,*], An Qin[a,**]

[a] Shanghai Key Laboratory of Orthopedic Implants, Department of Orthopaedics, Shanghai Ninth People's Hospital, Shanghai Jiaotong University School of Medicine, Shanghai, 200011, China
[b] Department of Nuclear Medicine, Shanghai Tenth People's Hospital, Tongji University School of Medicine, Shanghai, 200072, China
[c] Hongqiao International Institute of Medicine, Shanghai Jiaotong University School of Medicine, 201103, China
[d] Center for Chemistry of High-Performance & Novel Materials, Department of Chemistry, Zhejiang University, Hangzhou, 310027, China
[e] MOE Key Laboratory of Macromolecular Synthesis and Functionalization, Department of Polymer Science and Engineering, Zhejiang University, Hangzhou, 310027, China
[f] School of Biomedical Sciences, The University of Western Australia, Perth, Western Australia, 6009, Australia

ARTICLE INFO

Keywords:
Breast cancer metastasis
Osteoclast
Furin
Bone targeting
Iron oxide nanoparticles

ABSTRACT

Breast cancer bone metastasis poses significant challenge for therapeutic strategies. Inside the metastatic environment, osteoclasts and tumor cells interact synergistically to promote cancer progression. In this study, the proprotein convertase furin is targeted due to its critical roles in both tumor cell invasion and osteoclast function. Importantly, the furin inhibitor is specifically delivered by bone targeting superparamagnetic iron oxide (SPIO) nanoparticles. Our *in vitro* and *in vivo* data demonstrate that this system can effectively inhibit both osteoclastic bone resorption and breast cancer invasion, leading to alleviated osteolysis. Therefore, the bone targeting & furin inhibition nanoparticle system is a promising therapeutic and diagnostic strategy for breast cancer bone metastasis.

1. Introduction

Breast cancer is the most common cancer in women [1]. It has been estimated that 80% of advanced breast cancer patients will develop debilitating bone metastases [2], resulting in drastic reduction in the quality of life for patients. Once breast cancer bone metastasis occurs, the tumor cells and bone cells will interact synergistically to create favorable environment for metastasis growth and bone destruction [3]. Metastatic breast cancer cells regulate osteoblastic bone formation and osteoclastic bone resorption, which in turn positively feedback to potentiate tumor cell growth and survival. This creates a vicious cycle of elevated bone turnover and increased proliferation of cancer cells [4].

Furin, a member of proprotein convertases (PCs), contains a catalytic serine protease domain of the subtilisin type that is capable of cleaving specific basic amino acid motifs [5], serving as important function for the activation of various precursor proteins [6]. Elevated expression of Furin has been reported in many tumors and cancer cell lines [7] including breast cancer [8], and its upregulation is correlated with the aggressiveness of the tumor cell lines. Furin has also been found to uniquely activate Ac45, an accessory subunit of the vacuolar H^+-ATPase proton pump, which is indispensable for bone resorptive function of osteoclasts [9]. Additionally, Furin has been found to regulate pro-osteocalcin proteolysis and bone endocrine function in osteoblasts [6a]. Thus, Furin is considered to be a potential target for the development of specific inhibitors for the treatment of osteolytic bone destruction mediated by metastatic breast cancer cells.

In current therapeutic regimens, anti-cancer drugs cannot be adequately delivered to bone, because the unique characteristics of this tissue represses the penetration efficiency of therapeutic agents. The development of nano-constructs [10], including various nanoparticles, liposomes, and polymers, serves smart and multifunctional platforms [11] which are capable of carrying therapeutic agents to target cancer cells and generating *in vivo* images for diagnosis [12]. Superparamagnetic iron oxide (SPIO) nanoparticles are promising drug

Peer review under responsibility of KeAi Communications Co., Ltd.
* Corresponding author.
** Corresponding author.
E-mail addresses: profzhaojie@126.com (J. Zhao), Dr_qinan@163.com (A. Qin).
[1] Yichuan Pang, Li Su contribute equal to this work.

https://doi.org/10.1016/j.bioactmat.2020.09.006
Received 20 May 2020; Received in revised form 24 August 2020; Accepted 11 September 2020

carriers because of their T2 and T1 contrast effect for magnetic resonance imaging, high biocompatibility, stable colloidal suspensions *in vivo* [13], and flexible surface functionalities [14]. Several types of SPIO nanoparticles have been approved by United States Food and Drug Administration (FDA) for clinical uses [15]. In addition, SPIO nanoparticles can be biodegraded and metabolized and therefore do not accumulate in the body [16].

To treat breast cancer bone metastasis, a special bioactive moiety has to be installed on SPIO nanoparticles to target bone tissues. Small acidic peptides consisting of repeated sequences of aspartic acid (Asp) [17] have shown to preferential bind to hydroxyapatite, the main inorganic composition of bone. In this study, the surface of SPIO nanoparticles have been conjugated with a peptide containing a repeat sequence of glutamic acid-lysine-aspartic acid which can enhance the circulation of nanoparticles in the blood stream (the alternating-charge peptide poly EK could increase the stability of protein [18] and was considered as a nonfouling peptide [19]). We further attached a matrix metallopeptidases (MMPs) 2/9 responsive linker [20] to Furin inhibitory peptide to further enhance the specificity of the nanoparticles. The MMP2/9 is an enzymatic responsive trigger which is activated by invasive/metastatic phenotype as one of the crucial elements of tumor progression. At the same time, MMPs, in particular MMP9, are also crucial enzymes in the bone resorption process. Thus, a multifunctional and multiresponsive SPIO systems has been developed which can specifically target to bone metastatic sites, release the Furin inhibitory peptide through MMP2/9 triggered cleavage, and generate contrast for MRI imaging resulting in theranostic anti-cancer and anti-osteoclastic effects. (see Scheme 1)

2. Materials and methods

2.1. Reagents and media

All chemicals used to modify the super-paramagnetic iron oxide (SPIO) nanoparticles were purchased from Shanghai Aladdin Bio-Chem Technology Co. Ltd (Shanghai, China). Bare SPIO nanoparticles were obtained from Muke Nano Technology (Nanjing China), which was functionalized with HS-PEG_{2000}-NH_2 with a 2 mM amino group concentration in 1 mg/mL SPIO nanoparticles suspentsion. MMP-responsive and bone-targeting peptides were synthesis by GL Biochem Ltd (Shanghai, China). Dulbecco's Modified Eagle Media (DMEM), Minimum Essential Medium Eagle-Alpha Modification (αMEM), RPMI1640, fetal bovine serum (FBS), and penicillin/streptomycin were purchased from Gibco (Thermo Fisher Scientific, Waltham, MA, USA). 4′,6-diamidino-2-phenylindole (DAPI), Rhodamine-conjugated phalloidin, and fluorescein isothiocyanate (FITC) were obtained from Invitrogen (Thermo Fisher Scientific). Recombinant mouse M-CSF and mouse RANKL were purchased from R&D Systems (Minneapolis, MN, USA). Tartrate-resistant acid phosphatase (TRAP) staining kit was from Sigma-Aldrich (St Louis, MO, USA). Specific antibodies against CD86, CD11b, CD206 and F4/80 used in FACS analysis were obtained from eBioscience (Thermo Fisher Scientific). Specific antibodies against total and phosphorylated forms of p38, ERK, and JNK, and against GAPDH were purchased from Cell Signaling Technology (Danvers, MA, USA).

2.2. Synthesis of MMP-responsive furin inhibitory and bone-targeting peptide-conjugated SPIO nanoparticles

SPIO nanoparticles were obtained by classical ferric oleate route. Than, oleic acid groups were exchanged with citrate via incubating the system in 1,2-dichlorobenzene and DMF (v/v = 1:1) for 24 h at 100 °C. Bare SPIOs (PEG coated but without peptide modified) were harvested from decration the SPIO with functional HS-PEG_{2000}-NH_2 by exchange of citrate molecules with thiols. The amino groups on the surface of bare SPIO nanoparticles was measured by potentiometric titration. Bare SPIO nanoparticles were washed three times with ultrapure water and then centrifuged at 20,000 rpm for 1 h at 4 °C. The nanoparticles were then resuspended in 2 mM of 6-maleimidohexanoic acid followed by EDC/NHS coupling reaction for 48 h with constant stirring. At the end of the coupling reaction, nanoparticles were washed three times with ultrapure water and then pelleted by centrifugation at 20,000 rpm for 1 h at 4 °C. Pelleted nanoparticles were resuspended in water and reacted with MMP-responsive Furin-inhibitory and/or bone-targeting peptides for 24 h at a 1:2 (active group on nanoparticles:peptide) molar ratio at 4 °C with gentle agitation. The sequence for the MMP-responsive Furin-inhibitory peptide and bone-targeting peptide were CGGPLGVRGKRDRDRDRDRDRD (RD6) and CEKEKEKEKEKEKEKEKD-DDDDDD (C(EK)8D7) respectively. The peptide-conjugated nanoparticles (FI@SPIO – nanoparticles with RD6 peptide; BT-FI@SPIO – RD6 peptide and bone-targeting peptide) suspension were washed three

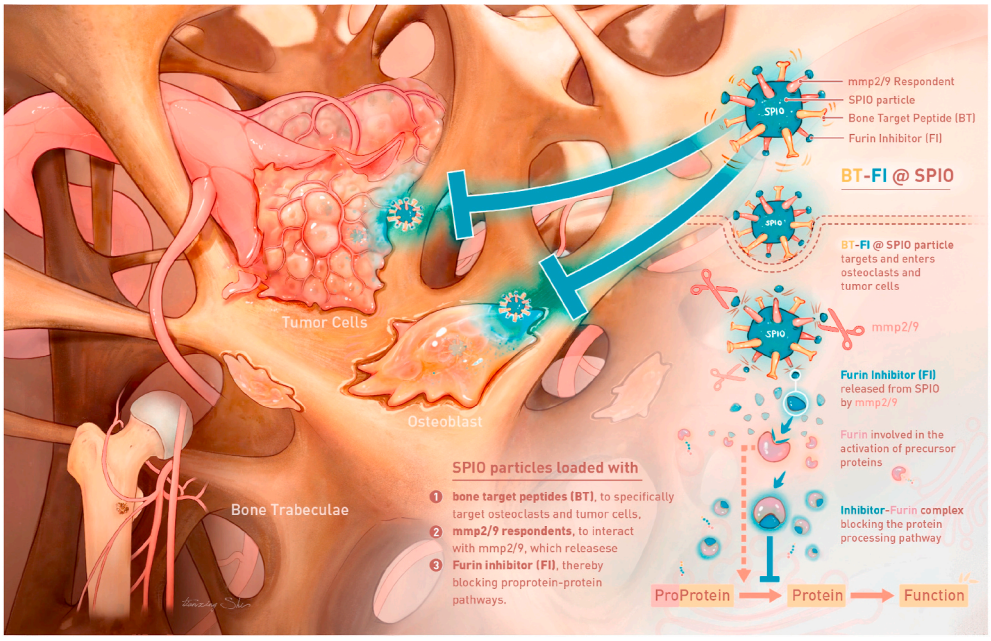

Scheme 1. Schematic illustration of bone targeting furin inhibitory SPIO nanoparticles for therapy towards breast cancer skeletal metastasis.

times with ultrapure water, centrifuged and resuspended in 0.9% NaCl for downstream applications.

2.3. Characterization of peptide-conjugated SPIO by transmission electron microscopy (TEM)

Nanoparticles suspension was diluted and dispensed onto a carbon-coated copper grid. Excess liquid was absorbed using filter paper and air-dried at room temperature. HR TEM was performed using a Hitachi HT7700 transmission electron microscope equipped with dual mode objective lens (Tokyo, Japan) at 100 kV. For the examination of nanoparticles in cells, nanoparticles-treated bone marrow macrophages (BMMs) were pelleted by centrifugation, mixed 1:1 with 2% low-gelling temperature agarose and then fixed in 2.5% glutaraldehyde at 4 ˚C overnight. Cells were then post-fixed with osmium tetroxide for 90 min at room temperature and dehydrated with cold graded ethanol series (15mins per change of: 30%, 50%, 70%, 80%, 90%, 95%, 100% ethanol). Samples were then washed with 100% acetone three times for 20 min each and then infiltrated with acetone/final Spurr resin mixture for 2–4 h on rotating mixer and then embedded in final Spurr resin in molding blocks overnight at 70 ˚C. Embedded samples were then subjected to ultramicrotomy for preparation of ultrathin sections with thickness under 100 nm on a Leica ultramicrotome (Leica Microsystems, Wetzlar, Germany). Sections were set on a carbon-coated copper grid and TEM performed using a JEM 2100F Field Emission electron microscope (JEOL Ltd, Tokyo, Japan).

2.4. Fourier Transform Infrared (FTIR) spectroscopy

Characterization of surface speciation of peptide-conjugated nanoparticles (FI@SPIO and BT-FI@SPIO) were conducted using FTIR. Nanoparticles were washed in water, pelleted by centrifugation and freeze-dried. Nanoparticles samples were mixed with potassium bromide powder, and the mixture were pressed into a transparent tablet. FTIR spectra for each nanoparticles sample were recorded on an FTIR spectrometer (Thermo Fisher Scientific) in transmission mode scanning within the range of 400–4000 cm^{-1}.

2.5. Animal ethics statement

All animals used and experiments conducted in this study were approved and performed in accordance with the Institution of Animal Care and Use Committee and under the supervision of Ninth People's Hospital affiliated to Shanghai Jiao Tong University School of Medicine. All animals were maintained in plastic micro-isolator cages (5 mice/cage) under specific pathogen-free conditions with a 12 h light/dark cycle at regulated temperatures of 22–24 ˚C and 50–55% humidity. Standard commercial mouse chow and water were provided ad libitum. All animals were acclimatized for 7 days prior to their participation in experiments.

2.6. Cell culture

BMMs were extracted from 4 to 6 weeks old C57BL/6 mice by marrow flushing of excised long bones and isolated cells were cultured in complete αMEM (αMEM containing 10% FBS and 1% penicillin/streptomycin) supplemented with 30 ng/mL M-CSF. For *in vitro* generation of osteoclasts, M–CSF–dependent BMMs were stimulated with 100 ng/ml RANKL without or with 100 ng/ml nanoparticles for 5–6 days until large multinucleated osteoclasts were formed. Cells were fixed with 4% paraformaldehyde (PFA) and stained for TRAP activity. Peritoneal macrophages were extracted from 4 to 6 weeks old C57BL/6 mice after 3 days of once daily intraperitoneal injection of 1 ml LB medium containing 5% starch. Mice were sacrificed on the 4th day and 5 ml of ice-cold RPMI1640 medium was injected into the peritoneal cavity. The abdomen was gently massaged for 5 min after which the RPMI1640 medium in the peritoneal cavity was extracted and peritoneal macrophages pelleted by centrifugation. Extracted peritoneal macrophages were maintained in RPMI1640 medium containing 10% FBS and 1% penicillin/streptomycin (10000U/ml). The human breast cancer cell line MDA-MB-231 and subline MDA-MB-231SArfp (expressing red fluorescence protein, RFP) with enhanced *in vivo* ability to spread and grow in bone were maintained in complete DMEM (DMEM containing 10% FBS and 1% penicillin/streptomycin). Cell culture media were changed every 2 days and all cells were maintained in a humidified environment of 37 ˚C and 5% CO_2.

2.7. In vitro cellular uptake of SPIO

The cellular uptake of SPIO by BMMs, BMM-derived osteoclasts, and MDA-MB-231 breast cancer cells were assessed by TEM and confocal microscopy. BMMs were treated with 100 ng/ml bare nanoparticles or peptide-conjugated nanoparticles (FI@SPIO or BT-FI@SPIO) for 2 or 24 h, and then processed for TEM analysis as described above. For confocal microscopy analysis, BMM-derived osteoclasts cultured on bovine bone discs and MDA-MB-231 cells cultured on glass coverslips were treated with 100 ng/ml FITC-labeled peptide-conjugated nanoparticles (FI@SPIO or BT-FI@SPIO) for 12 h. Cells were then fixed in 4% PFA for 20 min, permeabilized with 0.1% Triton X-100 for 5 min and then stained with Rhodamine-conjugated phalloidin for 1 h at room temperature in the dark. Nuclei were counterstained with DAPI for 5 min at room temperature in the dark. Samples were then mounted in anti-fade mounting media on glass slides and fluorescence images were captured on an Leica TCS SP8 confocal microscope (Leica Microsystems, Wetzlar, Germany).

2.8. Tumor cells migration and invasion evaluation

The inhibitory effect of SPIO nanoparticles on tumor cell migration and invasion was evaluated using the transwell migration/invasion and scratch-wound migration assays. For transwell migration assay, 5×10^4 MDA-MB-231 cells were seeded into the upper chamber of each transwell insert (24-well insert; pore size of 8 μm; Corning Inc, Corning, NY USA) in the absence or presence of 100 ng/ml bare SPIO nanoparticles or peptide-conjugated nanoparticles (FI@SPIO or BT-FI@SPIO) in serum-free DMEM. Next complete DMEM (containing 10% FBS) were added to the lower chamber of the 24-well plate and cells incubated for 12 h at 37 ˚C. For transwell invasion assay, upper chambers of each transwell insert were coated with 100 μl of diluted Matrigel (BD, USA) solution at 37 ˚C for 2 h. MDA-MB-231 cells were seeded and treated as described in the transwell migration assay above. At the end of the experimental period, the upper chamber inserts were rinsed with phosphate buffered saline (PBS) and gentle wiped with cotton swabs to remove non-migrating/non-invasive cells. Migrated cells were gently washed with PBS and then fixed in 4% PFA for 15 min and then stained with 0.1% crystal violet. The number of cells that migrated/invaded to the underside of the membrane were imaged under light microscopy at 5 random fields and quantified using ImageJ. Three independent experiments were carried out in triplicate.

For the scratch-wound migration assay, MDA-MB-231 cells were seeded into a 24-well plate at a density of 5×10^4 cells/well in complete DMEM and were allowed to grow to form a confluent monolayer. Using a sterilized pipette tip, a scratch-wound was made across the diameter of the well and cell monolayer. Cellular debris and floating cells were removed by gentle washing with PBS. Cells were then incubated with fresh culture media (serum-free DMEM) without or with 100 ng/ml bare SPIO nanoparticles or peptide-conjugated nanoparticles (FI@SPIO or BT-FI@SPIO) for 4 days. Immediately after the addition of fresh media, phase contrast images of each cell scratch-wound were captured and used as a starting reference point (day 0) for the percentage of cells that migrated into the scratch-wound area following the 4-day culture period.

2.9. MDA-MB-231 tumor cell viability/proliferation assay

The cleared conditioned media collected from polarized macrophages were used in MDA-MB-231 cell viability/proliferation assay. MDA-MB-231 cells seeded in 96-well plates were treated with cleared conditioned media for 1, 2 and 3 days. At each time point, the proliferation of tumor cells was measured with MTS assay in accordance with manufacturer's protocol (Promega, Madison, WI, USA). The absorbance of MTS was measured by Tecan M200Pro Absorbance Spectrophotometer at 490 nm (Tecan Trading AG, Switzerland).

2.10. Cleavage of RD_6 peptide from FI@SPIO nanoparticles in response to MMP2

The MMP-responsive Furin inhibitory peptide (RD_6) coated SPIO (FI@SPIO) were washed three times with ultrapure water, pelleting by centrifugation at 20,000 rpm after each wash. The FI@SPIO were re-suspended in 50 μl of ultrapure water in the 1.5 mL Eppendorf tubes. MMP2 was then added to the FI@SPIO to a final concentration of 10 μg/ml and incubated at 37 °C for 2 h with gentle agitation. After 2 h, that the system was pelleted by centrifugation at 20,000 rpm and the supernatant was subjected to HPLC analysis. The pure CGGPLGVRGK-RDRDRDRDRDRD and RDRDRDRDRDRD peptide solution was used as reference control.

2.11. Targeting of peptide-conjugated nanoparticles to bone-tumor site – in vivo MRI detection

The *in vivo* capacity of peptide-conjugated nanoparticles to target to bone-tumor sites were evaluated in BALB/c nude mice. To generate bone metastasis mice model, 100 μl of MDA-MB-231 breast cancer cells (density of 1×10^6 cells/ml) were injected directly in the tibial plateau of 6-week-old BALB/c nude mice (n = 6 per group) via a percutaneous approach. After 1-week of post-operative observation, mice were intraperitoneally injected with bare SPIO nanoparticles or peptide-conjugated nanoparticles (FI@SPIO or BT-FI@SPIO) twice per week for 2 weeks. After the experimental procedures, all mice had free access to food and water. MRI imaging of bone-tumor site was carried out on anesthetized mice 1 and 2 weeks after nanoparticles injection on a Bruker BioSpec 7T MRI scanner (Bruker, Billerica, MA, USA).

2.12. Targeting of bone targeting nanoparticles (BT-FI@SPIO) to bone surface

The *in vivo* capacity of bone-targeting nanoparticles (BT-FI@SPIO) labeled with FITC to target to bone surface was evaluated in C57BL/6 mice. To this end, 6-week old C57BL/6 (n = 6 per group) were intraperitoneally administered with alizarin red (20 mg/kg bodyweight) and BT-FI@SPIO^{FITC} (5 mg/kg bodyweight) or alizarin red with FITC probe alone (control group) every day for 3 days. After treatment, all mice had free access to food and water. At the end of the experimental period, all mice were sacrificed and the tibial bones were excised, cleaned of soft tissues, and fixed in 4% PFA. Fixed tibial bones were then processed for embedding in methyl methacrylate (MMA) according to standard protocol and sectioned at a thickness of 5 μm on a Leica Microtome (Leica Microsystems RM2255 Automated Microtome). Fluorescence images were captured on a Leica TCS SP8 confocal microscope (Leica Microsystems).

2.13. Ex vivo bone binding assay

To further test the affinity of the peptide-conjugated nanoparticles for bone, an *ex vivo* bone binding assay was performed. Long bones from C57BL/6 mice were excised, removed of soft tissues and the marrows flushed with ultrapure water. The cleaned bones were grinded into powdered form and then mixed with bare SPIO nanoparticles or peptide-conjugated nanoparticles (FI@SPIO or BT-FI@SPIO) for 12 and 24 h on a rocker mixer. The nanoparticles -bone mixture was then centrifuged and the Iron (Fe) atom to bone powder ratio of the pelleted fraction was measured by Energy-dispersive X-ray spectroscopy (EDX) (Hitachi High-Technologies, Tokyo, Japan). The supernatant fraction was analyzed for unbound nanoparticles by UV–Visible Spectroscopy.

2.14. In vitro bone mineral binding assay

The adhesion between bone-like substrates and the bone-targeting peptide (CEKEKEKEKEKEKEKDDDDDDD; $C(EK)_8D_7$) was demonstrated using an *in vitro* bone mineral binding assay. In brief, the bone-targeting peptide was incubated with hydroxyapatite powder (HAp with $CA_{10}(PO_4)_6(OH)_2$) for 2 h on a rocker mixer. The mixture was then centrifuged at 5000 rpm to pellet the peptide-bound HAp powder. The peptide-bound HAp powder fraction was then subjected to solid state nuclear magnetic resonance (ssNMR) analysis on a 600 MHz Bruker Avance III HD NMR spectrometer with a magnetic field strength of 14.1 T and resonance frequency of 100 MHz for ^{13}C. A Bruker 3.2 mm double-resonance magic-angle spinning (MAS) probe head was used at room temperature under 15 kHz MAS conditions. Pure bone-targeting peptide was used as the control comparison group.

2.15. In vivo evaluation of the efficacy of peptide-conjugated nanoparticles in an intratibial model of cancer-induced bone destruction

Six-week-old female BALB/c nude mice (n = 30) were anesthetized by intraperitoneal administration of ketamine (0.2 mL/100 g body weight) followed by intratibial injection of 100 μl MDA-MB-231SArfp cells (density of 5×10^6 cells/ml in PBS) into the tibial plateau of the left tibiae of mice. The contralateral tibiae were similarly injected with PBS as a control. After one week of post-operative observation, mice were randomly divided into 5 groups (n = 6 per group) and intraperitoneally injected with either PBS (Sham control group), RD_6 peptide (1 mg/kg), bare SPIO (1 mg/mL, 100 μL), FI@SPIO (1 mg/mL, 100 μL), or BT-FI@SPIO (1 mg/mL, 100 μL) every 2 days for 4 weeks. The weight, tumor size, and leg size of both limbs in each treatment group were recorded weekly. No fatalities were observed after tumor cell injection or nanoparticles administration, and the mice maintained regular activity throughout the duration of the experiment. Real-time non-invasive monitoring of MDA-MB-231SArfp breast cancer cell growth in the bone tissues after 4 weeks were imaged using the IVIS spectrum small-animal *in vivo* imaging system (IVIS Spectrum, PerkinElmer, USA). Mice were then sacrificed, and tumor legs and major organs including heart, liver, lung, and kidney were excised. Tumor legs (tibia) from each treatment group were processed for micro-CT and all tissues were processed for histological assessment.

2.16. Micro-CT, bone histology and TUNEL analyses

The resected tibial bones were analyzed using the SkyScan 1072 high-resolution μCT scanner (Bruker) with image acquired at a voltage of 70 kV, an electric current of 80 μA and an isometric resolution of 9 μm. After 3-dimensional reconstruction using NRecon software (SkyScan, Aartselaar, Belgium), a square region of interest set 0.5 mm below the tibia growth plate was selected for qualitative and quantitative analysis. Trabecular bone volume/tissue volume (BV/TV, %) were measured for each sample using CTAn software (Skyscan).

Following micro-CT, tumor tibial bones and all extracted tissues were fixed in 4% PFA for 48hrs followed by decalcification (bone tissues only) in 10% EDTA for 3 weeks. Tissues were then dehydrated and embedded in paraffin for thin tissue sectioning. Tissue sections were prepared for hematoxylin-eosin (H&E), tartrate resistant acid phosphatase (TRAP), and TUNEL staining.

2.17. Statistical analysis

A minimum sample number (n) of three for *in vitro* cellular and biochemical assessments and 6 for *in vivo* animal experiments were used to ensure statistical power. All the data are expressed as mean ± standard deviation (mean ± SD) of at least three independent experiments. Statistical difference was evaluated by Student's *t*-test or one-way analysis of variance (ANOVA) using GraphPad Prism software (San Diego, CA, USA). *P* values less than 0.05 (*), less than 0.01 (**), or less than 0.001 (***) were considered statistically significant.

3. Results and discussion

3.1. Furin regulates osteoclast differentiation and function

Furin has been shown to regulate the proteolytic processing of osteocalcin prohormone to mature active osteocalcin in osteoblasts [6a]. However, the role for Furin in osteoclast (OC) formation and bone resorption has been poorly explored. Among the proprotein convertase that were assessed, the gene expression of Furin was found to be the most highly and specifically expressed in both monocytic precursor cells (pre-OC) and mature OC (Fig. S1a). In comparison the gene expression of the tested proprotein convertase in the brain was relatively ubiquitous (Fig. S1b). As a previous report demonstrated the importance of Furin in osteoblasts, we compared the gene expression of Furin in osteoblasts and osteoclasts. Interestingly, we found that Furin was expressed at a 5-fold higher level in mature osteoclasts than in monocytic precursor cells and osteoblastic cells (Fig. S1c). Those results suggest that Furin may play a much greater role in osteoclast-lineage cells particularly in mature osteoclasts than in osteoblastic cells.

As such lentiviral-based gene knockdown experiments were conducted to assess the effects of Furin knockdown on osteoclast formation. As shown in Fig. S5, the gene knockdown of Furin markedly inhibited multinucleated osteoclast formation, indicating that Furin is functionally required for osteoclast formation. We next tested the efficiency of our MMP-responsive Furin inhibitory peptide (CGGPLGVRGKRDRDR-DRDRDRD; RD_6) that we used for coating of SPIO nanoparticles in subsequent experiments. We found that peptides containing the repeat sequence of arginine-aspartic acid (RDRDRDRDRDRD) as stable effective peptide inhibitors of Furin activity (Fig. S6b). The maturation process of Matrix Metallopeptidase 14 (MT1-MMP/MMP14) which was known as a substrate [21] of furin was inhibited after treatment with RD_6. More importantly, the RD_6 peptide showed no cellular cytotoxicity in bone marrow monocytes (BMMs) at the concentration of up to 50 μM and treatment for up to 4 days (Fig. S6a). Incubation of the RD_6 peptide during RANKL-induced osteoclast formation however significantly inhibited TRAP-positive multinucleated osteoclast formation at 1 μM (Fig. S6c, top panels). Higher peptide concentrations did not increase the inhibitory effect of the peptide (Fig. S6c). Similarly, bone resorptive function of mature osteoclasts on bone discs and bone-mimicking hydroxyapatite-coated OsteoAssay culture plates were inhibited in a somewhat dose-dependent manner (Figs. S6c–e). Immunoblot analysis further showed that the RD_6 peptide inhibited RANKL-induced activation of MAPK signaling pathways, ERK, JNK and p38 (Fig. S7). Collectively, these *in vitro* results indicate that Furin is important for osteoclast formation and bone resorption.

We then examined the potential *in vivo* effect of the RD_6 peptide in a mouse model of ovariectomy (OVX)-induced bone loss. Micro-CT 3D reconstruction of extracted tibias exhibited extensive bone loss in trabecular bone in OVX mice, whereas mice that received high-dose RD_6 peptide showed significant improvement in trabecular bone architecture and bone mass (Fig. S8). Collectively, our *in vivo* data suggests that the bone targeting Furin-inhibitory RD_6 peptide can exert osteoprotective effects against OVX-induced bone loss by inhibiting osteoclast formation and bone resorption.

3.2. Furin inhibitory peptide inhibits tumor cell migration and invasion

It is well established that proprotein convertases (PCs), particularly Furin, plays an important role in cancer metastatic process. Here we investigated the inhibitory potential of our RD_6 peptide against breast cancel migration and invasion *in vitro*. As shown in Fig. S9, inhibition of Furin activity by RD_6 peptide dose-dependently inhibited MDA-MB-231 breast cancer cell invasion through matrigel and migration through transwell membranes. A potent and dose-dependent inhibitory effect on cellular migration of MDA-MB-231 cells in the scratch-wound assay was similarly observed (Fig. S9). Thus, these data confirm that Furin is required for the invasive and metastatic potential of MDA-MB231 breast cancer cells and that our RD_6 peptide is a non-cytotoxic yet potent and efficient peptide inhibitor of Furin function.

3.3. Characterization of peptide-conjugated nanoparticles

Having now established the efficacy of the Furin inhibitory RD_6 peptide, we sought to incorporate the RD_6 peptide onto SPIO nanoparticles to generate a more effective drug/peptide delivery system. Here we prepared peptide-conjugated SPIOs by modifying SPIO nanoparticles either with MMP responsive Furin-inhibitory peptide (RD_6:CGGPLGVRGKRDRDRDRDRDRD; referred to as FI@SPIO) or with RD_6 and bone-targeting peptide ($C(EK)_8D_7$: CEKEKEKEKEKEKEKEKD-DDDDDD; referred to as BT-FI@SPIO). The morphology for formed nanoparticles was analyzed by transmission electron microscopy (TEM). As shown in Fig. 1a, peptide-conjugated SPIO exhibited a rougher outer surface layer than bare SPIO and in general nanoparticles in each group appears to be of uniform size (Fig. 1b). Dynamic light scattering (DLS) measurements of SPIO nanoparticles size before and after peptide conjugation (FI@SPIO or BT-FI@SPIO) further show enlargement of nanoparticles as a result of surface conjugation of peptides (Fig. 1c). Furthermore, by Fourier Transform Infrared (FTIR) spectra analysis (Fig. S2c), we demonstrated that the absorptive peaks of FI@SPIO and BT-FI@SPIO corresponded to the absorptive peaks of RD_6 and RD_6 + $C(EK)_8D_7$ peptides respectively. The successful conjugation of the peptides onto SPIO were further confirmed by the change in surface zeta potential of the nanoparticles (Fig. 1b). A rich content of PEG on the surface of bare SPIO nanoparticles gives it a relatively negative surface zeta potential (~ -50 mV). Conjugation of the Furin inhibitory RD_6 peptide resulted in the shielding of these PEG surface led to an increase in surface zeta potential to around -2 mV in FI@SPIO group. Interestingly, further conjugation of the bone targeting $C(EK)_8D_7$ which is rich in glutamic acid and aspartic acid sequences brought the zeta potential back down to ~ -35 mV (Fig. 1b). TEM/EDX measurements further proved the presence of the peptides on SPIO nanoparticles (Fig. S2c). What's more, there was more organic components in FI@SPIO and BT-FI@SPIO groups (32% and 47% respectively) compared with bare SPIO nanoparticles (18%) when using thermogravimetric analysis (TGA) (Fig. 1d). Taken together, these data confirmed the successful conjugation of the two peptides on SPIO nanoparticles (Fig. 1).

Ex vivo bone binding (bone targeting) tests were then conducted. Excised long bones from C57BL/6 mice were grinded into powder and then mixed with bare SPIO, FI@SPIO or BT-FI@SPIO for 12 and 24 h. Mixture was centrifuged and the Iron (Fe) content to bone powder ratio of the SPIO-bone aggregate fraction was measured by Energy-dispersive X-ray spectroscopy (EDX) and the supernatant fraction was analyzed for unbound SPIO using UV–Visible spectroscopy (Fig. 1f). Binding of the SPIO to bone powder resulted in decrease in OD reading in the supernatant fraction as a result of reduced SPIO concentration (and hence reduced colouration of supernatant) and a concomitant increase in Fe content in the SPIO-bone aggregates due to increased SPIO concentration in this fraction. As expected, a much greater proportion of BT-FI@SPIO was found to bind to the bone powder as compared to bare SPIO and FI@SPIO without the bone-targeting peptide.

The RD_6 peptide contains a MMP2/9 cleavable sequence that is

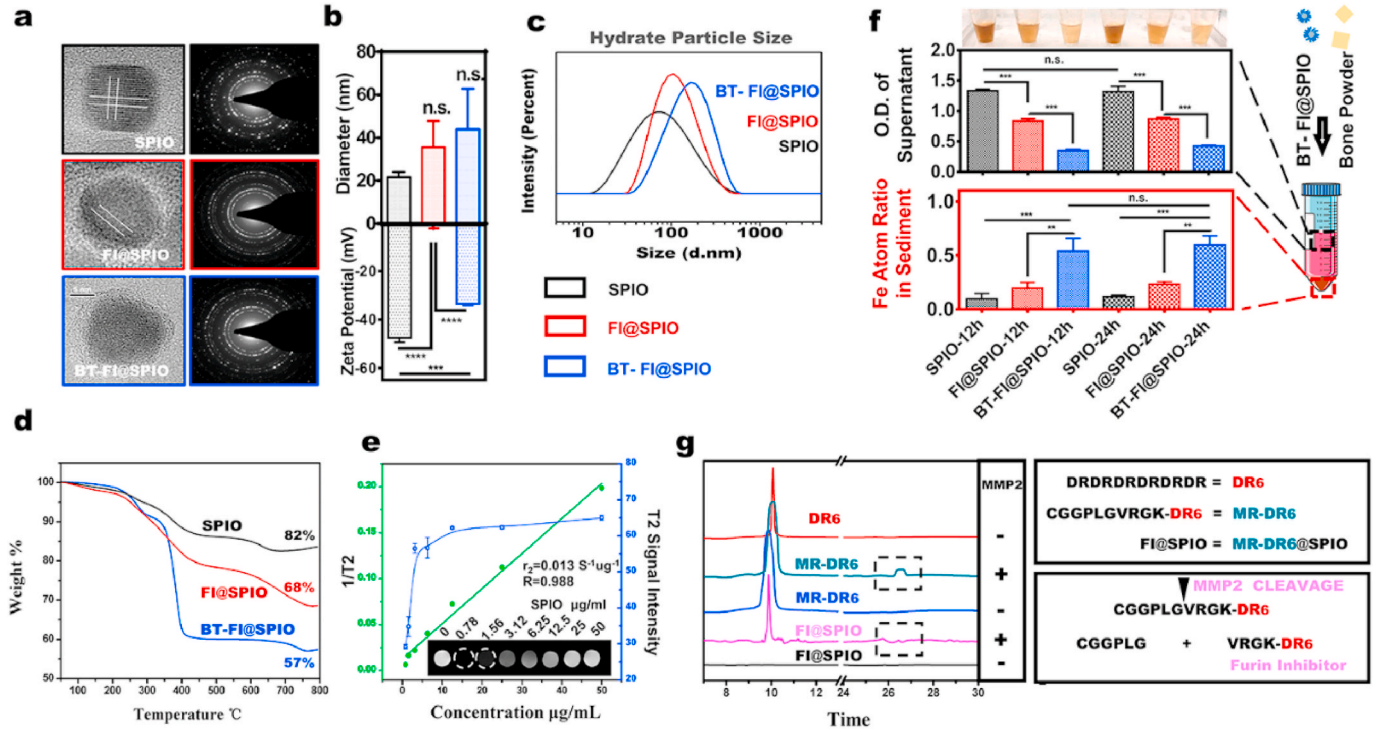

Fig. 1. Characterization of bone affinity and mmp2/9 triggered SPIO nanoparticles. (a) Diameter and surface potential; (b) TEM image; (c) relaxation time; (d) TGA of SPIO nanoparticles; (e) mmp2 responsive ability assay by HPLC; (f) diameter distribution of SPIO; (g) bone targeting ability *in vitro*.

important for the processing and release of the Furin inhibitory peptide when the BT-FI@SPIO are successfully delivered. To confirm that the conjugated RD_6 peptide on SPIO can be processed by MMP2/9 to release the Furin inhibitory peptide, FI@SPIO as well as RD_6 were incubated with/without MMP2 and the resulting reaction was subjected to HPLC analysis. As demonstrated in Fig. 1g, FI@SPIO in the absence of MMP2 exhibits no peak whereas FI@SPIO incubate with MMP2 showed 1 peak suggesting the cleavage of the RD_6 peptide and the release of the active Furin inhibitory peptide. However, bare RD_6 peptide incubate with MMP2 showed 2 peaks indicating two products cleaved by Furin.

3.4. Uptake of peptide-conjugated SPIO by BMMs/OCs and tumor cells

To be an effective drug delivery system, nanoparticles loaded with the specific cargo first needs to be endocytosed by the target cells. The cellular uptake of peptide-conjugated SPIO were examined by TEM and confocal microscopy in BMMs, actively resorbing mature osteoclasts, and in MDA-MB-231 breast cancer cells. As shown in the TEM micrographs in Fig. 2a, we can see the endocytic uptake of the bare SPIO and peptide-conjugated SPIO (FI@SPIO and BT-FI@SPIO) by BMMs within 2 h of exposure to the SPIO. Within 24 h the amount of SPIO that were engulfed by the BMMs was significantly elevated with numerous nanoparticles scattered throughout the cytoplasm of the cells. No cellular cytotoxicity (Fig. 2a) or organellar damage was observed, indicating that the SPIO were not toxic to the cells.

We next examined the uptake of the peptide-conjugated SPIO by actively resorbing osteoclasts. Mature osteoclasts cultured on bovine bone discs were exposed to FITC labeled SPIO (FI@SPIO and BT-FI@SPIO labeled with FITC) and then the cellular uptake and localization of the SPIO were assessed by confocal microscopy. As with BMMs, mature osteoclasts were capable of the endocytic uptake of the FITC labeled SPIO nanoparticles (Fig. 2b). However, osteoclasts exposed to FI@SPIO or BT-FI@SPIO appears to be morphologically compromised when compared to control osteoclasts. Furthermore, they do not possess well defined F-actin rings which are cytoskeletal phenomena indicative of the polarized state of osteoclasts actively undergoing bone resorption. This is consistent with our earlier bone resorption assays where the RD_6 peptide inhibited osteoclast bone resorption given that both FI@SPIO and BT-FI@SPIO is coated with the RD_6 peptide. Next, we examined the uptake of the peptide-conjugated SPIO by MDA-MB-231 breast cancer cells. As with BMMs and mature osteoclasts, MDA-MB-231 breast cancer cells can effectively uptake the peptide-conjugated SPIO nanoparticles without showing signs of morphological distress and little cytotoxic effects (Fig. 2b).

3.5. Peptide-conjugated SPIO inhibit osteoclast differentiation, and tumor cell migration and invasion in vitro

As BMMs were found to significantly uptake the peptide-conjugated SPIO we thus examined whether this affected their ability to differentiate into multinucleated osteoclasts. To this end, BMMs were stimulated with RANKL in the absence or presence of bare SPIO, FI@SPIO or BT-FI@SPIO for the duration of osteoclast differentiation. As shown in Fig. 2c,h and i, BMMs cultured in the presence of FI@SPIO or BT-FI@SPIO showed significant reduction in the number of $TRAP^{+ve}$ multinucleated osteoclasts formed (FI@SPIO reduction by 58% and BT-FI@SPIO reduction by 75%) as compared with untreated or bare SPIO treated controls. Treatment of cells with bare SPIO did not affect their capacity to form osteoclasts further attesting that the inhibitory effects of FI@SPIO and BT-FI@SPIO is the consequence of inhibition of Furin activity by the RD_6 peptide present of these SPIO nanoparticles. In addition, The migration of MDA-MB-231 cancer cells through the transwell membrane (Fig. 2d and j) and invasion through the matrigel (Fig. 2e) were significantly inhibited when cells were cultured in the presence of FI@SPIO or BT-FI@SPIO, with cells culture with BT-FI@SPIO showing stronger inhibitory effect. In a similar manner, lower migratory capacity was also observed in the scratch-wound migration assay (Fig. 2f, g and k). MDA-MB-231 cells treated with bare SPIO showed little inhibitory effect in cell migration and invasion which further attest that the observed inhibitory effect is due to impairment of Furin function in MDA-MB-231 cells.

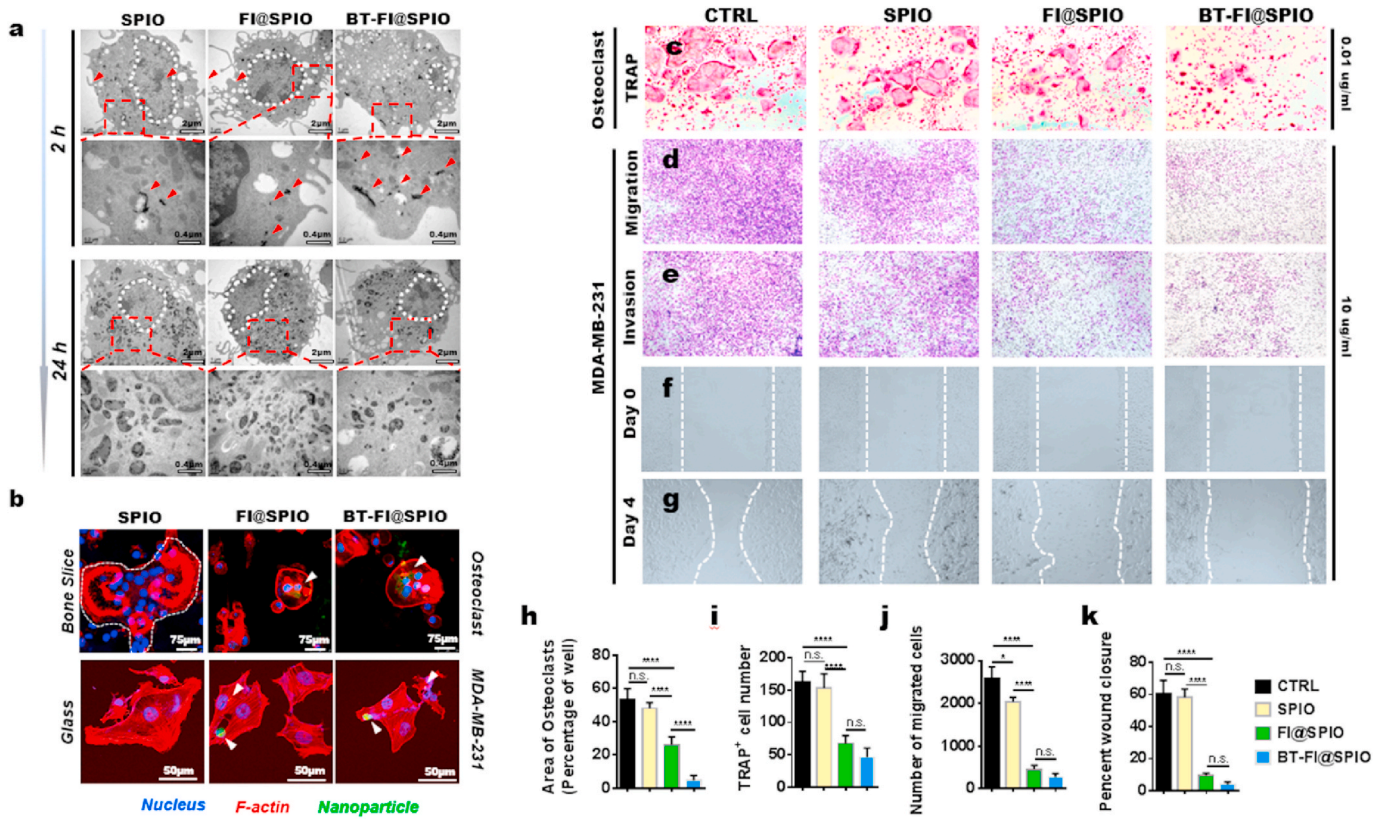

Fig. 2. Biological effect of BT-FI@SPIO. (a) TEM and (b) confocal images of the BMMs, osteoclasts and breast cancer cells uptaking SPIO nanoparticles; (c) TRAP staining of osteoclasts; (d) migration, (e) invasion and (f–g) scratch assay of MDA-MB-231 breast cancer cell; (h) area and (i) number of TRAP positive multinucleate cells in (e); (j) migration cell in (d); (k) healing area of scratch assays in (g).

3.6. Targeting of BT-FI@SPIO to bone tissues

To achieve active targeting of SPIO nanoparticles it is necessary to conjugate targeting agents onto the nanoparticles surface directly so as to localize adequate levels of SPIO at a disease site. We first showed that the bone-targeting peptide ($C(EK)_8D_7$) exhibits high affinity binding to the hydroxyapatite component of bone using an *in vitro* bone mineral hydroxyapatite (HAp) binding assay and solid state NMR analysis (Fig. 3a). In the 13C spectra, the carboxylate signals (~180 ppm) of the peptide shift to upfield when it is coupled to the Hap nanoparticles. We expect that SPIO nanoparticles modified with $C(EK)_8D_7$ can bee effectively deliverd to bone tissues. We evaluated the *in vivo* capacity of peptide-conjugated SPIO to target to bone-tumor sites using intratibial implants of MDA-MB-231 breast cancer cells in BALB/c nude mice. As shown in the MRI scans, mice administered with the BT-FI@SPIO bone targeting nanoparticles exhibit markedly reduced T2 MRI signals at the tumor-bone site 2 weeks post-operation (Fig. 3b). This suggests that BT-FI@SPIO could effectively target to the tumor-bone site where it exerted its inhibitory effect on target cells (MDA-MB-231) thereby reducing the tumor size and therefore T2 MRI signal. Although the T2 MRI signal were also observed to be weaker in mice treated with non-bone-targeting FI@SPIO and bare SPIO nanoparticle, it was not as significant as compared to the BT-FI@SPIO treated mice.

To exclude the possibility that the reduced T2 MRI signal in BT-FI@SPIO treated mice were the result of enhanced permeability and retention (EPR) effect of tumor tissues, we conducted *in vivo* fluorescence tracking of BT-FI@SPIO targeting to bone tissues. By using *in vivo* tracing image system (IVIS) , we study the bio-distribution of SPIO in different organs. The results shown in Fig. 3c, while SPIO, FI@SPIO and BT-FI@SPIO were mainly aggregation in liver, there are more nanoparticles affinity to bone in BT-FI@SPIO group. Further, C57BL/6 mice were administered alizarin red, a red fluorescent probe that binds strongly to bone tissues, together with FITC-labeled BT-FI@SPIO. As shown in Fig. 3d, accumulation of FITC-labeled BT-FI@SPIO (green) can be seen accumulating on the trabecular bone surface (red) of the tibial bone providing direct evidence for the specific targeting of BT-FI@SPIO to the bone tissues.

3.7. In vivo efficacy of peptide-conjugated SPIO against breast cancer bone metastases and osteolytic bone destruction

Finally, we examined the potential application of the Furin inhibitory peptide-conjugated SPIO as a therapeutic approach for the treatment of breast cancer bone metastases and osteolytic bone destruction. An intraosseous mouse model of bone metastases and osteolytic lesions were induced by intratibial inoculation of BALB/c nude mice with MDA-MB-231Srfp human breast carcinoma cell. After one week of observation, mice were treated with intraperitoneal injections of PBS (Sham control group), RD_6 peptide, bare SPIO nanoparticles, or with peptide-conjugated SPIO (FI@SPIO or BT-FI@SPIO) every 2 days for 4 weeks. No fatalities or unrelated adverse effects were observed after tumor cell implantation or treatment administration, and the mice maintained regular activity throughout the duration of the experiment. The *in vivo* imaging of tumor growth (represented by fluorescence intensity of the tumors) at the end of 4 weeks showed that tumor size was significant reduced in mice administered with BT-FI@SPIO, the SPIO conjugated with the bone targeting and Furin inhibitory peptides (Fig. 4a). Although not to the same extent as BT-FI@SPIO, mice administered with FI@SPIO (SPIO with Furin inhibitory peptide but no bone targeting peptide) also show reduced tumor size when compared to sham controls. The inhibitory effect of FI@SPIO at the bone-tumor site could be the result of EPR effect of tumor tissues suggested earlier. Mice administered with unconjugated Furin inhibitory peptide RD_6 or bare SPIO did not show significant reduction in fluorescence intensity

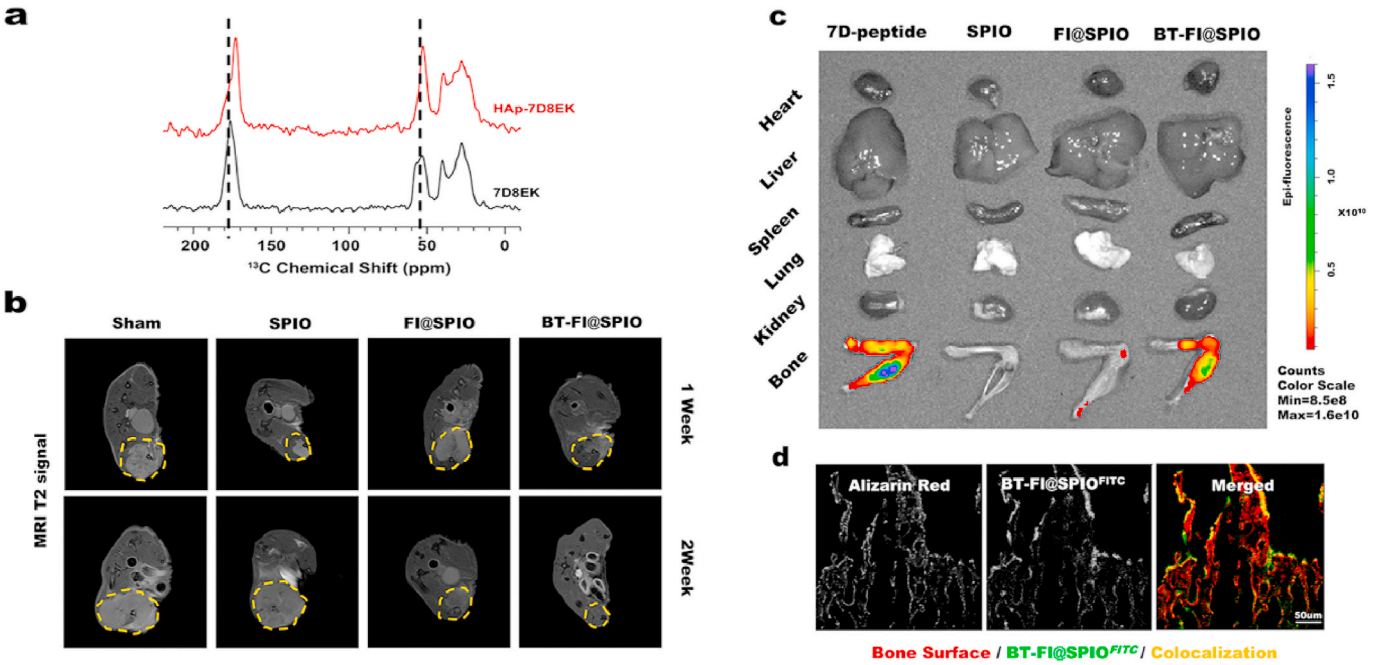

Fig. 3. In vivo bone targeting ability of BT-FI@SPIO. (a) Bone affinity mechanism of targeting peptide by solid state NMR; (b) tumor images of MRI, (c) bio-distribution and (d) hard tissue slice after treated with SPIO/FI@SPIO/BT-FI@SPIO.

with tumor size similar to Sham controls (Fig. 4b).

Osteolytic bone lesions were further analyzed using radiography and micro-CT analysis. As seen in the standard X-ray radiographs, severe bone lytic lesions and bone destruction at the tibial plateau were observed in Sham control mice as well as in mice administered with unconjugated RD_6 peptide or bare SPIO (Fig. 4c, yellow dot cycle). In contrast, in mice administered with BT-FI@SPIO, the osteolytic lesions and bone destruction was significantly attenuated. Again, FI@SPIO

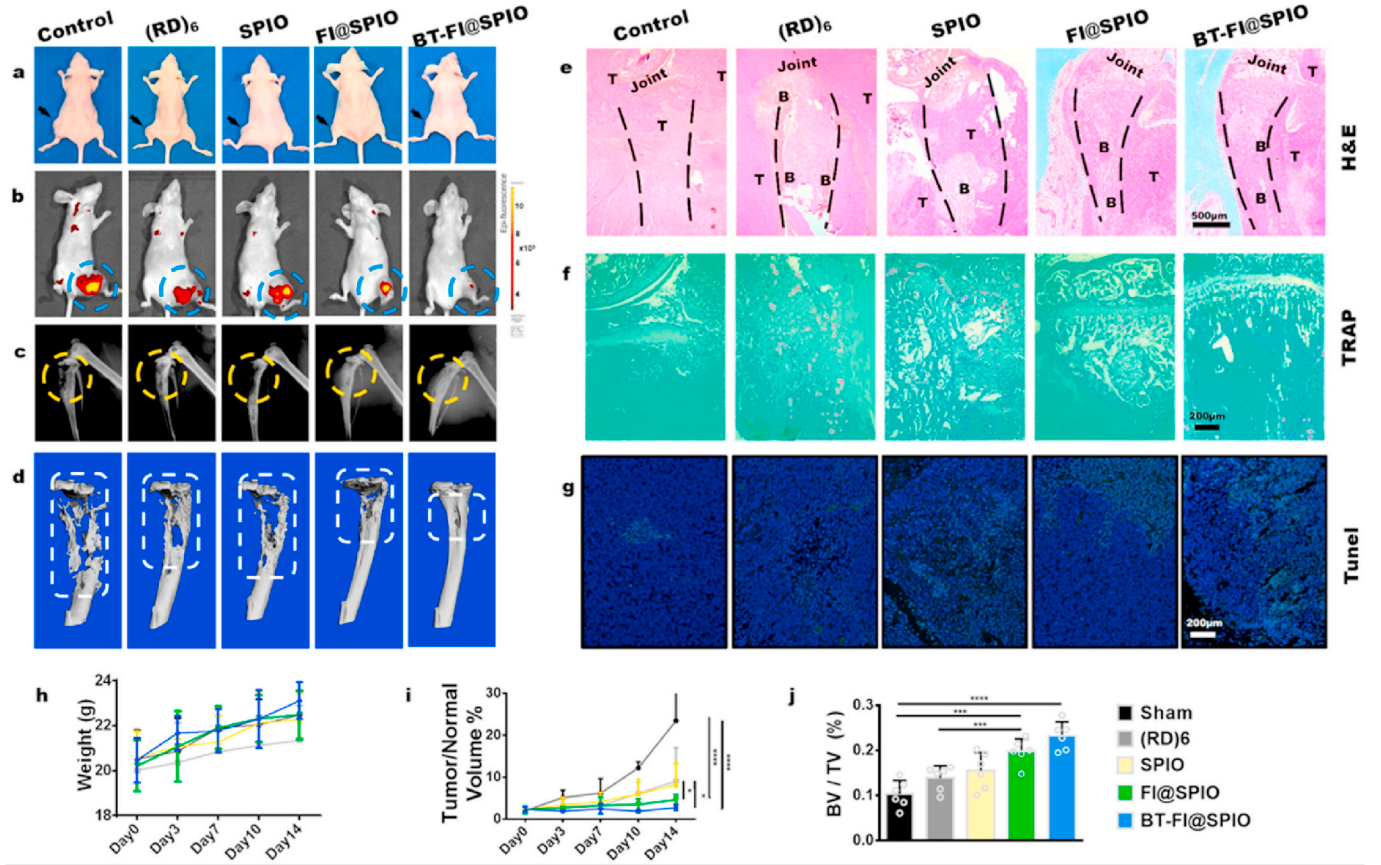

Fig. 4. In vivo effect of SPIO nanoparticles. (a) Gross images of tumor bearing mice; (b) In vivo images of tumor; (c) X-Ray and (d) micro-CT of each groups; (e)–(h) histological images of tumor skeletal metastasis. (e) HE staining, T = tumor and B = bone, (f) TRAP staining and (g) Tunel staining. (h) Mouse weight and (i) tumor volume, (j) microCT analysis of bone volume v.s. Tissue volume.

treatment reduced osteolytic bone destruction but not to the same degree as BT-FI@SPIO treatment. Three-dimensional microCT reconstructions further confirmed the findings of the X-ray radiographs (Fig. 4d). Quantitative morphometric analysis showed that BT-FI@SPIO and FI@SPIO treated mice exhibited on average 2.3 times and 1.8 times respectively, more bone volume (BV/TV, %) than Sham controls (Fig. 4j).

Histological assessment further showed the protective effects of BT-FI@SPIO against tumor cells induced osteolytic lesions. In H&E sections from Sham controls, RD6 and bare SPIO treated mice, extensive metaphyseal bone destruction was apparent with joint architecture severely destroyed or mutilated (Fig. 4e, H&E staining). Invasion and occlusion of trabecular and marrow space by tumor tissue was observed. In contrast, in the sections from the FI@SPIO and BT-FI@SPIO-treated mice, the overall joint architecture remains intact. However, only mice treated with BT-FI@SPIO maintained overall tibial bone architecture and integrity with intact cortical and trabecular bone. Some osteolytic lesions were still observed in FI@SPIO treated mice. But in generally, these results further demonstrate that the peptide-conjugated SPIO can effectively reduce bone destruction induced by metastatic cancer cells.

TRAP staining further showed that the number of osteoclasts at the interface between the tumor and bone were significantly reduced in BT-FI@SPIO and FI@SPIO treated mice (Fig. 4f, TRAP staining). On the other hand, abundant $TRAP^{+ve}$ osteoclasts were observed in sections from RD_6 peptide and bare SPIO treated mice. Unexpectedly, no TRAP positivity was observed in sections from the Sham controls and we believe that this is due to the lack of bone tissues left within the tumor-bone site and therefore no osteoclasts. Finally, TUNEL staining of apoptotic tumor cells showed a significant increase in the number of TUNEL-positive tumor cells in all of the SPIO treated groups in comparison to Sham controls and RD_6 peptide treated mice.

Collectively, the *in vivo* data provided strong evidence for the therapeutic use of peptide-conjugated SPIO nanoparticles in particular BT-FI@SPIO in the treatment of metastatic tumor-induced bone osteolysis. BT-FI@SPIO nanoparticles were targeted specifically to bone tissues where it attenuated osteoclast-mediated bone destruction.

4. Conclusion

In this study, we synthesized SPIO nanoparticles conjugated with bone targeting and Furin inhibitory peptide that is responsive to MMP cleavage. We showed that this system markedly inhibited tumor progression and alleviated osteoclast-mediated bone destruction. These encouraging functional investigations provide insight into therapeutic and diagnostic value of utilizing these multifunctional SPIO nanoparticles for bone metastatic breast cancer, but future research will need to be carried out focusing on elucidating more thoroughly the molecular mechanisms and other cellular effects that may be involved.

CRediT authorship contribution statement

Yichuan Pang: Writing - original draft, Visualization. **Li Su:** Validation. **Yao Fu:** Data curation, Methodology. **Fan Jia:** Investigation. **Chenxi Zhang:** Resources. **Xiankun Cao:** Investigation. **Wenxin He:** Resources. **Xueqian Kong:** Visualization, Conceptualization. **Jiake Xu:** Conceptualization. **Jie Zhao:** Conceptualization, Supervision. **An Qin:** Project administration, Funding acquisition, Writing - review & editing.

Declaration of competing interest

The authors declare that they have no known competing financial interests or personal relationships that could have appeared to influence the work reported in this paper.

Acknowledgements

This project is supported by grants from Natural Science Foundation of China (No.81772373, No.81572167), by Shanghai Municipal Education Commission -Gaofeng Clinical Medicine Grant Support, the SHIPM-pi fund No. JY201804 & No.JC201801 from Shanghai Institute of Precision Medicine, Ninth People's Hospital Shanghai Jiao Tong University,Shanghai Jiao Tong University School of Medicine, and by the Foundation of National Facility for Translational Medicine (Shanghai) (No.TMSK-2020-119).

Appendix A. Supplementary data

Supplementary data to this article can be found online at https://doi.org/10.1016/j.bioactmat.2020.09.006.

References

[1] a) J. Dittmer, Semin. Canc. Biol. 53 (2018) 59;
b) L.A. Torre, F. Bray, R.L. Siegel, J. Ferlay, J. Lortet-Tieulent, A. Jemal, CA Cancer J Clin 65 (2015) 87.
[2] R. Coleman, D.M. Finkelstein, C. Barrios, M. Martin, H. Iwata, R. Hegg, J. Glaspy, A.M. Periañez, K. Tonkin, I. Deleu, J. Sohn, J. Crown, S. Delaloge, T. Dai, Y. Zhou, D. Jandial, A. Chan, Lancet Oncol. 21 (2020) 60.
[3] a) Theresa A. Guise, Gregory R. Mundy, Endocr. Rev. 19 (1998) 18;
b) K.N. Weilbaecher, T.A. Guise, L.K. McCauley, Nat. Rev. Canc. 11 (2011) 411.
[4] a) T. Onishi, N. Hayashi, R.L. Theriault, G.N. Hortobagyi, N.T. Ueno, Nat. Rev. Clin. Oncol. 7 (2010) 641;
b) A. Tang, Y. Qian, S. Liu, W. Wang, B. Xu, A. Qin, G. Liang, Nanoscale 8 (2016) 10570.
[5] M.V. Andrea Stieneke-Grober, Herbert E.S. Angliker, Thomas2 Gary, Christopher Roberts, Hans-Dieter Kienk, W. Garten, EMBO J. 11 (1992) 2407.
[6] a) O. Al Rifai, J. Chow, J. Lacombe, C. Julien, D. Faubert, D. Susan-Resiga, R. Essalmani, J.W. Creemers, N.G. Seidah, M. Ferron, J. Clin. Invest. 127 (2017) 4104;
b) S. Nandadasa, C.M. Kraft, L.W. Wang, A. O'Donnell, R. Patel, H.Y. Gee, K. Grobe, T.C. Cox, F. Hildebrandt, S.S. Apte, Nat. Commun. 10 (2019) 953;
c) T.R. Cotton, G. Fischer, X. Wang, J.C. McCoy, M. Czepnik, T.B. Thompson, M. Hyvonen, EMBO J. 37 (2018) 367.
[7] a) N. Scamuffa, G. Siegfried, Y. Bontemps, L. Ma, A. Basak, G. Cherel, F. Calvo, N.G. Seidah, A.M. Khatib, J. Clin. Invest. 118 (2008) 352;
b) X. Sun, R. Essalmani, N.G. Seidah, A. Prat, Mol. Canc. 8 (2009).
[8] V. Kumar, R. Behera, K. Lohite, S. Karnik, G.C. Kundu, Canc. Res. 70 (2010) 10381.
[9] E. Louagie, N.A. Taylor, D. Flamez, A.J. Roebroek, N.A. Bright, S. Meulemans, R. Quintens, P.L. Herrera, F. Schuit, W.J. Van de Ven, J.W. Creemers, Proc. Natl. Acad. Sci. U. S. A. 105 (2008) 12319.
[10] a) X. Qin, H. Chen, H. Yang, H. Wu, X. Zhao, H. Wang, T. Chour, E. Neofytou, D. Ding, H. Daldrup-Link, S.C. Heilshorn, K. Li, J.C. Wu, Adv. Funct. Mater. (2018) 28;
b) Anming Tang, Yu Qian, Shuang Liu, Weijuan Wang, Bing Xu, An Qin, Gaolin Liang, Nanoscale 8 (2016) 10570.
[11] Z. Wang, X. Xue, Y. He, Z. Lu, B. Jia, H. Wu, Y. Yuan, Y. Huang, H. Wang, H. Lu, K.S. Lam, T.Y. Lin, Y. Li, Adv. Funct. Mater. 28 (2018).
[12] a) K. Pu, J. Huang, Y. Jiang, J. Li, S. He, J. Huang, Angew Chem. Int. Ed. Engl. (2019), https://doi.org/10.1002/anie.201911859;
b) J. Li, D. Cui, Y. Jiang, J. Huang, P. Cheng, K. Pu, Adv. Mater. (2019) 31;
c) K.Y. Choi, S. Correa, J. Min, J. Li, S. Roy, K.H. Laccetti, E. Dreaden, S. Kong, R. Heo, Y. H. Roh, E.C. Lawson, P.A. Palmer, P.T. Hammond, Adv. Funct. Mater. 29 (2019).
[13] J. Ward, J.A. Guthrie, M.B. Sheridan, S. Boyes, J.T. Smith, D. Wilson, J.I. Wyatt, D. Treanor, P.J. Robinson, J. Clin. Oncol. 26 (2008) 4304.
[14] F. Goodfellow, G.A. Simchick, L.J. Mortensen, S.L. Stice, Q. Zhao, Adv. Funct. Mater. 26 (2016) 3899.
[15] J.W.M. Bulte, Adv. Drug Deliv. Rev. 138 (2019) 293.
[16] V.P. Vu, G.B. Gifford, F. Chen, H. Benasutti, G. Wang, E.V. Groman, R. Scheinman, L. Saba, S.M. Moghimi, D. Simberg, Nat. Nanotechnol. 14 (2019) 260.
[17] G. Zhang, B. Guo, H. Wu, T. Tang, B.T. Zhang, L. Zheng, Y. He, Z. Yang, X. Pan, H. Chow, K. To, Y. Li, D. Li, X. Wang, Y. Wang, K. Lee, Z. Hou, N. Dong, G. Li, K. Leung, L. Hung, F. He, L. Zhang, L. Qin, Nat. Med. 18 (2012) 307.
[18] J. Smith, P. McMullen, Z. Yuan, J. Pfaendtner, S. Jiang, Biomacromolecules (2019), https://doi.org/10.1021/acs.biomac.9b01191.
[19] A.K. Nowinski, F. Sun, A.D. White, A.J. Keefe, S. Jiang, J. Am. Chem. Soc. 134 (2012) 6000.
[20] a) Q. Lei, W.X. Qiu, J.J. Hu, P.X. Cao, C.H. Zhu, H. Cheng, X.Z. Zhang, Small 12 (2016) 4286;
b) H. Han, D. Valdeperez, Q. Jin, B. Yang, Z. Li, Y. Wu, B. Pelaz, W.J. Parak, J. Ji, ACS Nano 11 (2017) 1281.
[21] V.S. Golubkov, A.V. Chekanov, S.A. Shiryaev, A.E. Aleshin, B.I. Ratnikov, K. Gawlik, I. Radichev, K. Motamedchaboki, J.W. Smith, A.Y. Strongin, J. Biol. Chem. 282 (2007) 36283.